energies as well, and furthermore that lattice studies have reached the stage where all systematic errors can be fully controlled. This will prove important in the forthcoming era in which lattice calculations will play a vital role in unraveling possible new physics from processes that are interlaced with QCD effects.

References and Notes

- 1. D. J. Gross, F. Wilczek, Phys. Rev. Lett. 30, 1343 (1973).
- 2. H. D. Politzer, Phys. Rev. Lett. 30, 1346 (1973).
- 3. K. G. Wilson, Phys. Rev. D Part. Fields 10, 2445 (1974).
- 4. S. Aoki et al., Phys. Rev. Lett. 84, 238 (2000).
- 5. S. Aoki et al., Phys. Rev. D Part. Fields 67, 034503 (2003).
- 6. C. T. H. Davies et al., Phys. Rev. Lett. **92**, 022001 (2004).
- 7. S. Aoki et al., http://arxiv.org/abs/0807.1661 (2008).
- C. W. Bernard et al., Phys. Rev. D Part. Fields 64, 054506 (2001).
- C. Aubin et al., Phys. Rev. D Part. Fields Gravit. Cosmol. 70, 094505 (2004).

- 10. N. Ukita et al., Proc. Sci. LAT2007, 138 (2007).
- 11. M. Gockeler et al., Proc. Sci. LAT2007, 129 (2007).
- 12. D. J. Antonio *et al.*, *Phys. Rev. D Part. Fields Gravit. Cosmol.* **75**, 114501 (2007).
- A. Walker-Loud et al., http://arxiv.org/abs/0806.4549 (2008).
- 14. L. Del Debbio, L. Giusti, M. Luscher, R. Petronzio, N. Tantalo, *J. High Energy Phys.* **02**, 056 (2007).
- 15. C. Alexandrou et al., http://arxiv.org/abs/0803.3190 (2008).
- 16. J. Noaki et al., Proc. Sci. LAT2007, 126 (2007).
- 17. M. Luscher, Commun. Math. Phys. 104, 177 (1986).
- 18. M. Luscher, Commun. Math. Phys. 105, 153 (1986).
- 19. See supporting material on Science Online.
- 20. M. Luscher, *Nucl. Phys. B* **354**, 531 (1991).
- 21. M. Luscher, Nucl. Phys. B 364, 237 (1991).
- 22. G. Colangelo, S. Durr, Eur. Phys. J. C 33, 543 (2004). 23. A. Ali Khan et al., Nucl. Phys. B 689, 175 (2004).
- B. Orth, T. Lippert, K. Schilling, Phys. Rev. D Part. Fields Gravit. Cosmol. 72, 014503 (2005).
- 25. M. A. Clark, Proc. Sci. LAT2006, 004 (2006).
- 26. W. M. Wilcox, Proc. Sci. LAT2007, 025 (2007).
- 27. S. Durr et al., http://arxiv.org/abs/0802.2706 (2008).

- 28. W. M. Yao et al., J. Phys. G33, 1 (2006).
- C. Michael, A. McKerrell, *Phys. Rev. D Part. Fields* 51, 3745 (1995).
- 30. Computations were performed on the Blue Gene supercomputers at FZ Jülich and at IDRIS and on clusters at Wuppertal and CPT. This work is supported in part by European Union (EU) grant I3HP; Országos Tudományos Kutátasi Alapprogramok grant AT049652; Deutsche Forshungsgemeinschaft grants FO 502/1-2 and SFB-TR 55; EU grants RTN contract MRTN-CT-2006-035482 (FLAVIAnet) and (FP7/2007-2013)/ERC no. 208740; and the CNRS's GDR grant 2921. Useful discussions with 1. Charles and M. Knecht are acknowledged.

Supporting Online Material

www.sciencemag.org/cgi/content/full/322/5905/1224/DC1 SOM Text

Figs. S1 to S5 Tables S1 and S2 References

14 July 2008; accepted 1 October 2008

10.1126/science.1163233

4D Imaging of Transient Structures and Morphologies in Ultrafast Electron Microscopy

Brett Barwick, Hyun Soon Park, Oh-Hoon Kwon, J. Spencer Baskin, Ahmed H. Zewail*

With advances in spatial resolution reaching the atomic scale, two-dimensional (2D) and 3D imaging in electron microscopy has become an essential methodology in various fields of study. Here, we report 4D imaging, with in situ spatiotemporal resolutions, in ultrafast electron microscopy (UEM). The ability to capture selected-area-image dynamics with pixel resolution and to control the time separation between pulses for temporal cooling of the specimen made possible studies of fleeting structures and morphologies. We demonstrate the potential for applications with two examples, gold and graphite. For gold, after thermally induced stress, we determined the atomic structural expansion, the nonthermal lattice temperature, and the ultrafast transients of warping/bulging. In contrast, in graphite, striking coherent transients of the structure were observed in both image and diffraction, directly measuring, on the nanoscale, the longitudinal resonance period governed by Young's elastic modulus. The success of these studies demonstrates the promise of UEM in real-space imaging of dynamics.

lectrons, because of their wave-particle duality, can be accelerated to have picometer wavelength and focused to image in real space (1). With the impressive advances made in transmission electron microscopy (TEM), augmented by scanning and aberration-correction features, it is now possible to image with high resolution (2-7), reaching the sub-angstrom scale. Together with the progress made in electron crystallography, tomography, and single-particle imaging (8-13), today the electron microscope in different variants of two-dimensional (2D) and 3D recordings has become a central tool in many fields, from materials science to biology (14–16). For all conventional microscopes, the electrons are generated either thermally by heating the

electron beam is made of random single-electron bursts with no control over the temporal behavior. In these microscopes, time resolution of milliseconds or longer, being limited by the video rate of the detector, can be achieved, while maintaining the high spatial resolution, as demonstrated in environmental-TEM studies (17).

Ultrafast imaging, using pulsed photoelectron products provides approximation for studying in

cathode or by field emission, and as such the

Ultrafast imaging, using pulsed photoelectron packets, provides opportunities for studying, in real space, the elementary processes of structural and morphological changes. In electron diffraction, ultrashort time resolution is possible (18), but the data are recorded in reciprocal space. With nanosecond and submicron image resolutions (19, 20) limited by space charge, ultrashort processes cannot be observed. To achieve ultrafast resolution in microscopy, the concept of single-electron pulse imaging (18) was realized as a key to the elimination of the Coulomb repulsion between electrons while maintaining the high temporal and spatial resolutions. As long

as the number of electrons in each pulse is below the space-charge limit, the packet can have a few or tens of electrons, and the temporal resolution is still determined by the femtosecond (fs) optical pulse duration and the energy uncertainty, which is also on the fs time scale (21), and the spatial resolution is atomic scale (22). However, the goal of full-scale dynamic imaging can be attained only when, in the microscope, the problems of in situ high-spatiotemporal resolution for selected image areas and of heat dissipation (for reversible processes) are overcome.

Here, we present the methodology of ultra-fast imaging with applications in studies of structural and morphological changes in single-crystal gold and graphite films, which exhibit entirely different dynamics. For both, the changes were initiated by in situ fs impulsive heating, while image frames and diffraction patterns were recorded in the microscope at well-defined times after the temperature jump. The time axis in the microscope is independent of the response time of the detector, and it is established using a variable delay-line arrangement; a 1-µm change in optical path of the initiating (clocking) pulse corresponds to a time step of 3.3 fs.

Shown in Fig. 1 is a picture of the secondgeneration ultrafast electron microscope (UEM-2) built at the California Institute of Technology (Caltech). The integration of two laser systems to a modified electron microscope is indicated in the figure, together with a representative image showing the resolution of a 3.4 Å lattice spacing obtained in UEM without the field-emissiongun (FEG) arrangement of conventional TEM. In the figure, the fs laser system is used to generate the single-electron packets, whereas the ns laser system was used for both single-shot and stroboscopic recordings (23). In the single-electron mode of operation, as in UEM-1 (24), the coherence volume is well defined and appropriate for image formation in repetitive events (25). The dynamics are fully reversible, retracing an identical evolution after each initiating laser pulse; each image is constructed stroboscopically, in seconds,

Physical Biology Center for Ultrafast Science and Technology, Arthur Amos Noyes Laboratory of Chemical Physics, California Institute of Technology, Pasadena, CA 91125, USA.

^{*}To whom correspondence should be addressed. E-mail: zewail@caltech.edu

from typically 10⁶ pulses, and all time frames are processed to make a movie. The time separation between pulses can be varied to allow complete heat dissipation in the specimen.

In the hundreds of images collected for each time scan, the dynamics was followed for area-specific changes, giving rise to selectedarea-image dynamics (SAID) and selected-areadiffraction dynamics (SADD); for the former, in real space, from contrast change, and for the latter, in Fourier space, from changes of the Bragg peak separations, amplitudes, and widths. It is the advantage of microscopy that allows us to perform this "parallel-imaging" dynamics with pixel resolution, when compared with diffraction, in this case up to one part in 4 million (2048 × 2048 pixels). As shown below, it would not have been possible to observe the selected temporal changes if the total image were to be averaged over all pixels. Neither could we have resolved the ultrafast dynamics if the time resolution were nanoseconds or longer.

In Fig. 2, A and B, we display representative time-framed images of the gold nanocrystal using the fs excitation pulses at a repetition rate of 200 kHz and peak excitation fluence of ~1.7 mJ/cm² with an estimated spot diameter of 60 µm. In the first image, taken at -84 ps, before the clocking pulse (t = 0), typical characteristic features, such as bend contours, of the single crystal gold are observed in the image. Bend contours, which appear as broad fuzzy dark lines in the image, are diffraction contrast effects occurring in warped or buckled samples of constant thickness (26). In the dark regions, the zone axis (the crystal [100]) is well aligned with the incident electron beam and electrons are scattered efficiently, whereas in the lighter regions, the alignment of the zone axis deviates more and the scattering efficiency is lower. Because bend contours generally move when deformation causes tilting of the local crystal lattice, they provide in images a sensitive visual indicator of the occurrence of such deformations.

At positive times, after t = 0, visual dynamical changes are observed in the bend contours (Fig. 2B). A series of such image frames with equal time steps provides a movie of the morphological dynamics (Movie S1). To more clearly display the temporal evolution, image-difference frames were constructed. Depicted as insets in Fig. 2B are those obtained when referencing to the -84 ps frame for t = +66 ps and +151 ps. In the difference images, the regions of white or black indicate locations of surface morphology change (bend contour movement), whereas gray regions are areas where the contrast is unchanged from that of the reference frame. The white and black features in the difference images are nanometer-scale, reflecting the local dynamics of deformations. Care was taken to ensure the absence of long-term specimen drifts because they can cause apparent contrast change.

To quantify the changes in the image, we used the following method of cross-correlation. The

normalized cross-correlation of an image at time *t* with respect to that at time *t'* is expressed as

$$\gamma(t';t) = \frac{\sum_{x,y} C_{x,y}(t) C_{x,y}(t')}{\sqrt{\sum_{x,y} C_{x,y}(t)^2 \sum_{x,y} C_{x,y}(t')^2}}$$
(1)

where the contrast $C_{x,y}(t) = [I_{x,y}(t) - \bar{I}(t)]/\bar{I}(t)$; $I_{xy}(t)$ is the intensity of the pixel at the position of (x,y) at time t, and $\bar{I}(t)$ is the mean of $I_{xy}(t)$. This correlation coefficient $\gamma(t';t)$ is a measure of the temporal change in "relief pattern" between the two images being compared, which can be used as a guide to image dynamics as a function of time. Two types of cross-correlation plots were made, those referenced to a fixed-image frame before t=0 and those that show correlation between adjacent time points. (Another quantity that shows time dependence qualitatively similar to that of the image cross-correlation is the standard deviation of pixel intensity in difference images).

Shown in Fig. 2, C and D, are the cross-correlation values between the image at each measured time point and a reference image recorded before the arrival of the clocking pulse. The experiments were repeated (for different time-delay steps of 500 fs, 1 ps, 5 ps, and 50 ps), and similar results were obtained (Fig. 2C), showing that morphology changes are completely reversible and reproducible over each 5-µs interpulse interval. The adjacent-time cross-correlations reveal the time scales for intrinsic changes in the images, which disappear for time steps below 5 ps, consistent with full-image rise in time (27). Over all pixels, the time scale for

image change covers the full range of time delay, from picoseconds to nanoseconds, indicating the collective averaging over sites of the specimen; as shown in Fig. 2C, the overall response can be fit to two time constants of 90 ps and 1 ns.

The power of SAID is illustrated when the dynamics of the bend contours are followed in different selected areas of the image, noted in the micrographs as SAI #1, #2, and #3. The corresponding image cross-correlations (Fig. 2D) have different shape and amplitude from each other and from the full-image correlation. The large differences observed here and for other data sets, including onsets delayed in time (Fig. 2, G to L) and sign reversals, indicate the variation in local deformation dynamics. In Fig. 2, G to K, a timeresolved SAI at higher magnification is depicted. A broad and black "penguin-like" contour is observed as the dominant feature of this area. As shown in the frames, a colossal response to the fs heating is noted. The gray region inside the black contour appears and broadens with time. Also, a new black contour above the large central white hole begins to be evident at 1200 ps and gains substantial intensity over the following 50 ps; all frames taken construct a movie of SAID (Movie S2).

The observed SAID changes correspond to diffraction contrast (bright-field) effects in bend contours, as mentioned above. It is known that the shape of bend contours can be easily altered by sample tilting or heating inside the microscope. However, here in the UEM measurements, the changes in local tilt are transient in nature, reflecting the temporal changes of morphology and structure. Indeed, when the experiments were repeated in the TEM mode of operation, that is,

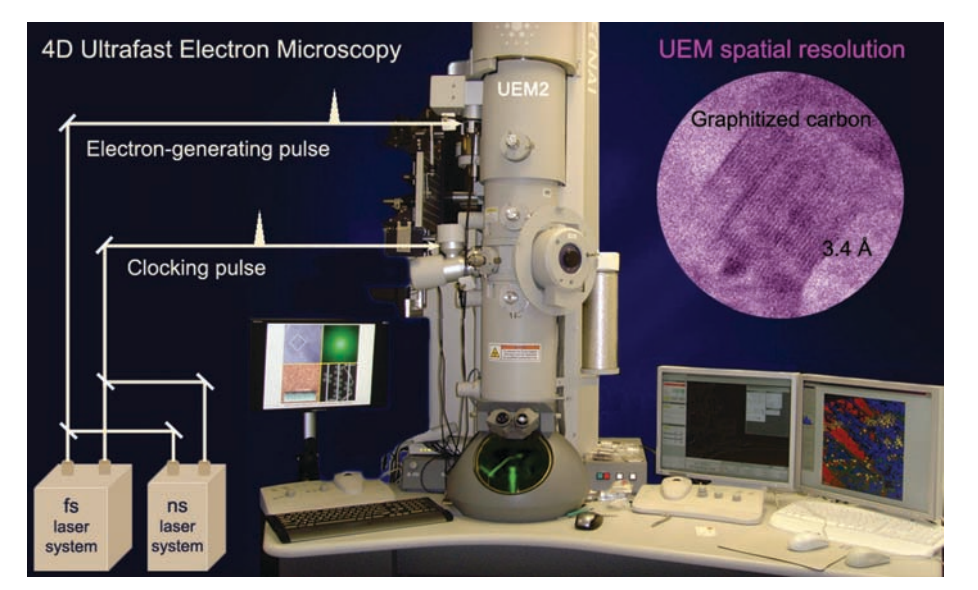


Fig. 1. Photograph of the UEM-2 microscope at Caltech, together with a high-resolution image of a graphitized carbon sample showing 3.4 Å lattice fringes. Displayed is the interface of two laser systems (fs and ns) to a modified, hybrid 200-kV TEM designed with two ports for optical access. It is straightforward to switch (by flipping two mirrors) between the laser systems to permit both fs and ns operation. The optical pulses are directed to the photocathode to generate electron packets, as well as to the specimen to initiate (clock) the change in images with a well-defined delay time Δt . The time axis is defined by variable delay between the electron generating and clocking pulses.

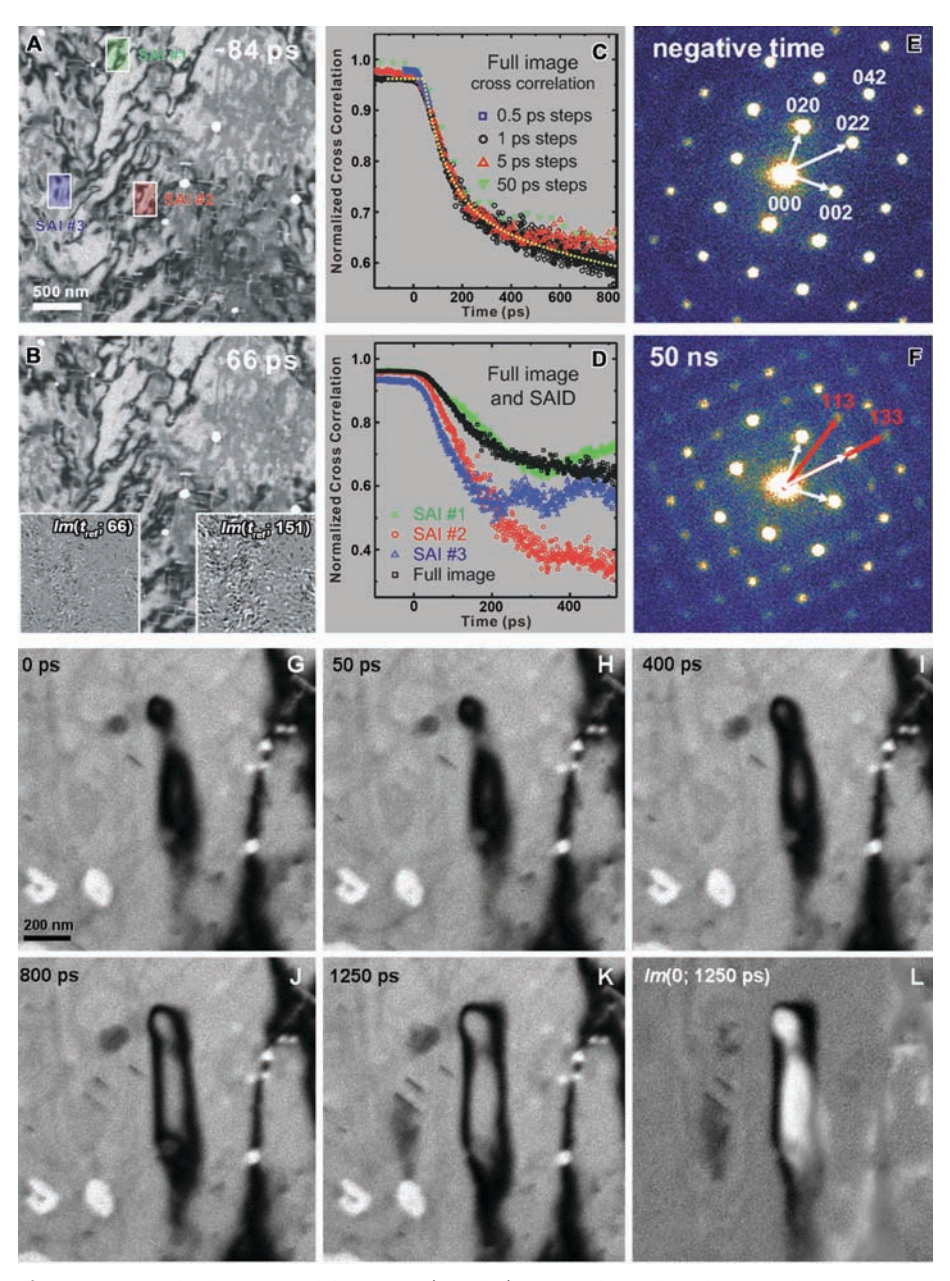


Fig. 2. Time-resolved images and diffraction. (A and B) Images obtained stroboscopically at two typical time delays after heating with the fs pulse (fluence of 1.7 m]/cm²). The gold specimen, 11 nm thick, was obtained from Ted Pella Inc.; the single-crystal film was mounted on a standard 3-mm 400-mesh grid. Shown are the bend contours (dark bands), and holes in the sample (bright white circles). The insets are image-difference frames $Im(t_{ref}; t)$ with respect to the image taken at -84 ps. The thickness was checked by EELS in our UEM-2. (C) Time dependence of image cross-correlations of the full image from four independent scans taken with different time steps. A fit to biexponential rise of the 1-ps step scan is drawn, yielding time constants of 90 ps and 1 ns. (D) The time dependence of image cross-correlations at 1-ps time steps for the full image and for selected areas of interest SAI #1, #2, and #3, as shown in the -84 ps image (A). (E and F) Diffraction patterns obtained using a single pulse of $\simeq 10^6$ electrons with high peak heating fluence (40 m]/cm²) and selected-area aperture of 25-µm diameter; two frames are given to indicate the change. Diffraction spots were indexed and representative indices are shown. (G to L) Highmagnification nanoscale image change with time. The sample normal is tilted at a 10° angle to the microscope axis. In these bright-field images (also in Fig. 2), the boundaries are assigned to the {111} twins of gold (36). Note the large change in the penguin-like contrast with time. The bright regions in the field of view correspond to holes locally damaged by laser heating above the threshold in previous experiments. (L) is a difference image, Im(0; 1250 ps), which properly eliminates reference and unchanged (with time) features, including holes.

for the same heating laser pulse and same scanning time but with continuous electron probe beam, no image change was observed. This is further supported by the change in diffraction observed at high fluences and shown in Fig. 2, E and F, for two frames, at negative time and at +50 ns; in the latter, additional Bragg spots are visible, a direct evidence of the transient structural change due to bulging at longer times.

Whereas real-space imaging shows the timedependent morphology, the SADD provides structural changes on the ultrashort time scale. Because the surface normal of the film is parallel to the [100] zone axis, the diffraction pattern of the sample was properly indexed by the facecentered-cubic (fcc) structure projected along the [100] zone axis at zero tilt angle (see the singlepulse diffraction pattern of Fig. 2E). From the positions of the transient spots in Fig. 2F, which are reflections from the {113} and {133} planes, forbidden in the [100] zone-axis viewing, we measured the interplanar spacings to be 1.248 and 0.951 Å, respectively. To reproduce the appearance of those peaks, we need to tilt the sample by an angle of more than 10° without laser heating. From stroboscopic SAD patterns, Bragg peak separations, amplitudes, and widths were obtained as a function of time. The results indicate different time scales from those of image dynamics.

The average amplitude of {042} diffraction peaks drops significantly; the rise time is 12.9 ps, whereas the change in average separation of all planes observed in the [100] zone axis is delayed by 31 ps and rises in 60 ps (Fig. 3A) (28). The delay in the onset of separation change with respect to amplitude change is similar to the time scale for the amplitude to reach its plateau value of 15% reduction in the case of the {042} amplitude shown. These structural dynamics are consistent with the electron and lattice temperature obtained by optical reflectivity (29). To determine the recovery time of the structure, we carried out stroboscopic (and also single-pulse) experiments over the time scale of microseconds. The recovery transient in the inset of Fig. 3A (at 7 mJ/cm²) gives a time constant of 2.2 μs; we made calculations of 2D lateral heat transport with thermal conductivity $\lambda = 3.17 \text{ W/(cm·K)}$ at 300 K and laser spot diameter of 60 µm, and reproduced the observed time scale.

The atomic-scale motions, which lead to structural and morphological changes, can now be visualized. Because the specimen is nanoscale in thickness, the initial temperature induced is essentially uniform across the atomic layers and heat can only dissipate laterally. It is known that for metals the lattice temperature is acquired after the large increase in electron temperature (30). The results in Fig. 3A give the temperature rise as 13 ps; from the known electron and lattice heat-capacity constants $[C_1 = 70 \text{ J/(m}^3 \cdot \text{K}^2)$ and $C_2 = 2.5 \times 10^6 \text{ J/(m}^3 \cdot \text{K})$, respectively] and the electron-phonon coupling $[g = 2 \times 10^{16} \text{ W/(m}^3 \cdot \text{K})]$, we obtained the initial heating time of ~10 ps for electron temperature $T_1 = 2500 \text{ K}$, in good

agreement with the observed rise (29). Reflectivity measurements do not provide structural information, but they give the temperature rise (29). For bulk material, the time scale for heating (\sim 1 ps) is shorter than that of the nanoscale specimen (\sim 10 ps), due to confinement in the latter, which limits the ballistic motion of electrons in the specimen (29), and this is evident in the UEM studies. Because the plane separation is 0.4078 nm, the change of the average peak separation (0.043%), at the fluence of 1.7 mJ/cm² of the fs pulse, gives a lateral lattice constant change of 0.17 pm.

Up to 30 ps, the lattice is hot but, because of macroscopic lattice constraint, the atomic stress cannot lead to changes in lateral separations, which are the only separations visible for the [100] zone-axis probing. However, the morphology warping change is correlated with atomic (lateral) displacements in the structure as it relieves the structural constraint. Indeed, the time scale of the initial image change is comparable to that of plane separations in diffraction (60 to 90 ps). This initial warping, which changes image contrast, is followed by longer time (nanosecond) minimization of surface energy and bulging, as shown in Fig. 2D. If the picometer-scale lateral structural change (0.17 pm) were applied to the thickness, the stress over the 11-nm specimen would give a total expansion of 4.7 pm. Considering the influence of the measured lateral expansion, the maximum bulge reaches 1 to 10 nm, depending on the lateral scale (31). Finally, the calculated Debye-Waller factor for structural changes gives a temperature of 420 K ($\Delta T =$ 125 K), in agreement with the lattice temperature derived under similar conditions, noting that for the nanoscale material the temperature is higher than in the bulk (29, 31).

Graphite, with its unique 2D structure and physical properties, was the second specimen studied in the application of the UEM methodology reported here. In contrast to the observations made for gold, in graphite, by off-axis selected-area recording, coherent resonance modulations in the image, and also in diffraction, were directly resolved in real time. The damped resonance of very high frequency, as shown below, has its origin in the nanoscale dimension of the specimen and its elasticity. The initial fs pulse induces an impulsive stress in the film and the ultrafast electron tracks the change of the transient structure, both in SAID and SADD. In Fig. 3, B and C, we display the diffraction pattern and the results obtained by measuring changes of the diffraction spot $(1\overline{2}2)$ and, in Fig. 4 those obtained by dark-field (DF) imaging with the same diffraction spot being selected by the objective aperture. The specimen was tilted at a 21° angle to the microscope axis, and the diffraction pattern was indexed along the [011] zone axis. With different magnifications, Moiré (fig. S1) and buckling fringes are observed in the images (Fig. 4).

For both the image and the diffraction, a strong oscillatory behavior is evident, with a welldefined period and decaying envelope. When the

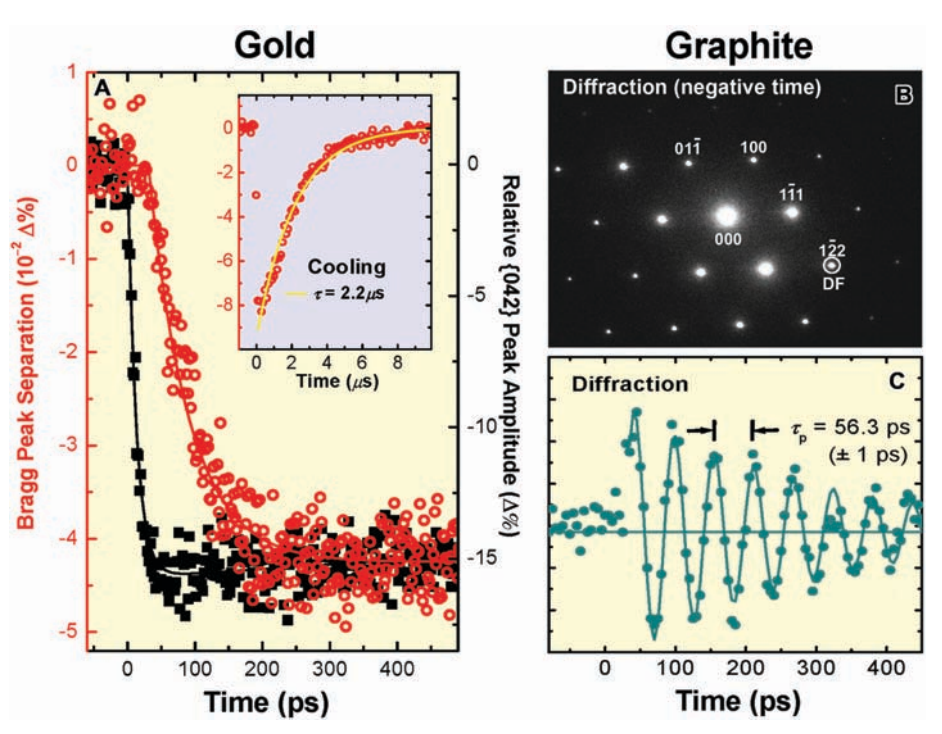


Fig. 3. Structural dynamics and heat dissipation in gold, and coherent resonance of graphite. (A) SADD for fs excitation at 1.7 m]/cm² peak fluence (519 nm). The Bragg separation for all peaks and the amplitude of the {042} peaks are shown in the main panel; the inset gives the 2.2-µs recovery (by cooling) of the structure obtained by stroboscopic ns excitation at 7 ml/cm². The peak amplitude has been normalized to the transmitted beam amplitude, and the time dependence of amplitude and separation is fit as an exponential rise, and a delay with rise, respectively. (B) The diffraction pattern of graphite taken at negative time, that is, before the arrival of the clocking pulse. The experiments were carried out with a natural single crystal of graphite on a grid. To prepare the specimen, a graphite crystal was glued to the grid and repeatedly cleaved. The glue was subsequently dissolved in acetone, and graphite flakes with varying dimensions were left on the grid, covering some of the grid squares completely. The graphite thickness for the data shown is 103 nm as determined by EELS in UEM-2. The specimen was tilted at a 21° angle to the microscope axis, and the diffraction pattern was obtained by using a SAD aperture of 6-µm diameter. The diffraction spots were indexed according to the hexagonal structure of graphite along the [011] zone axis, and representative indices are shown. The circled diffraction ($1\overline{2}$) spot is the one used for the DF imaging of Fig. 4. (C) Resonance oscillations observed for the Bragg $(1\overline{2}2)$ peak in the diffraction pattern of (B); the oscillation period (τ_p) is measured to be 56.3 ps. For a thickness of 64 nm, the period is 35.4 ps.

diffraction transient was fitted to a damped resonance function $[(\cos 2\pi t/\tau_p)\exp(-t/\tau_{decay})]$, we obtained $\tau_p = 56.3 \pm 1$ ps for the period. The decay of the envelope for this particular resonance is significantly longer; $\tau_{decay} = 280$ ps. This coherent transient decay, when Fourier transformed, indicates that the thickness variation of the film is only ± 3 nm (Eq 2.). The thickness of the film was determined (d = 103 nm) using electron energy loss spectroscopy (EELS) in our UEM (mean-free path of inelastic scattering of 150 nm).

To test the validity of this resonance behavior, we repeated the experiments for another thickness, d=64 nm. The period indeed scaled with d, giving $\tau_p=35.4$ ps. These hitherto unobserved, in real time, very-high-frequency resonances (30 gigahertz range) are unique to the nanoscale thickness of graphite. They also reflect the (harmonic) motions due to strain along the c-axis direction, because they were not observed when we repeated the experiment for the electron incident along the [001] zone axis. The fact that the period of the diffraction is the

same as that of the image suggests the direct correlation between local atomic structure and macroscopic elastic behavior.

After a femtosecond pulse of stress on an ideal freely vibrating nanofilm, oscillations are expected which are related to the velocity (υ) of acoustic waves between specimen boundaries, which in turn can be related to Young's modulus (Y) of the c axis (c_{33} elastic modulus):

$$\frac{1}{\tau_{\rm p}} = \frac{n \upsilon}{2d} = \frac{n}{2d} \left(\frac{Y}{\rho}\right)^{1/2} \tag{2}$$

where n is a positive integer, with n=1 being the fundamental resonance frequency (higher n's are for overtones). Knowing the measured τ_p 's and d's, we obtained $\upsilon=3.6\times10^5$ cm/s. For a graphite density $\rho=2.26$ g/cm³, Yequals 30 GPa for the c axis strain in the natural specimen examined, a value that is certainly in the range of the reported 20 to 47 GPa for c_{33} (32, 33). Pyrolytic graphite has Y values that range from about 10 to 1000 GPa, depending on the orien-

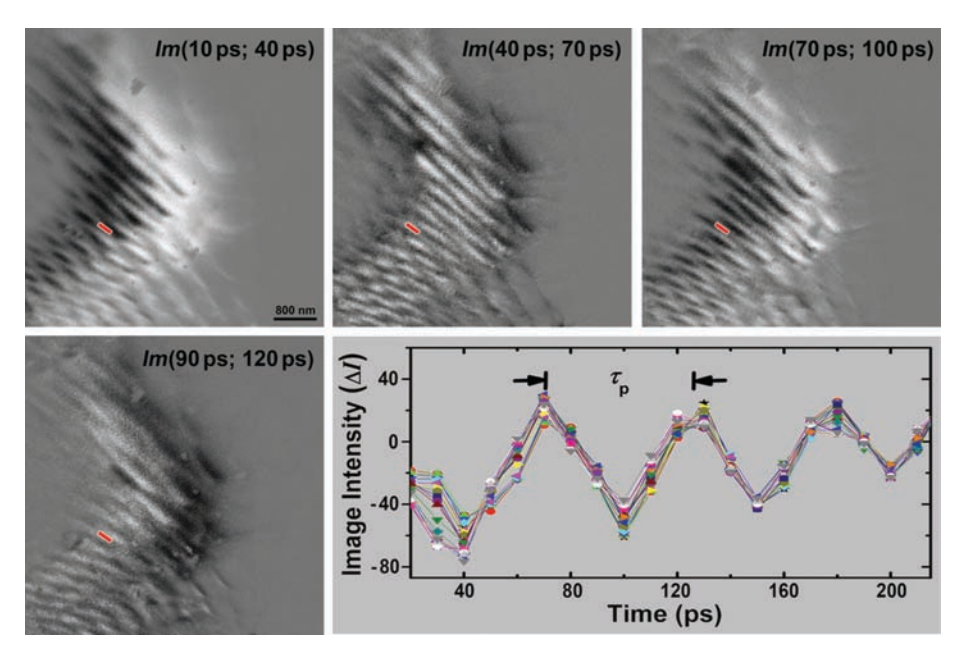


Fig. 4. Image, selected areas, and time dependence of intensity difference (DF) for graphite. Moiré fringes (37) were observed at high resolution (fig. S1), and their separations vary from 2.6 nm to 36.6 nm depending on the angle between two layers. The buckling fringes here are separated by ~300 nm but vary with location; the scanning tunneling microscopy—observed fringes (38) are on the scale of 150 nm, reflecting differences in (zone-axis) scattering (39, 40). Shown are several difference images, Im(t-30 ps; t), and a plot of SAI intensities. The difference images were constructed from a series of DF images obtained by selecting the Bragg ($1\overline{2}2$) spot circled in Fig. 3B. The selected areas for the intensity plot are indicated by the red box. The temporal evolution of the DF difference images clearly shows the resonance behavior, with time steps corresponding to the peak and trough in the intensity oscillations. Note the direct change in contrast with time and its recurrences at longer time. Each color in the intensity plot corresponds to a selected area of a 1 × 100-pixel slice parallel to contrast fringes in the DF image. The image change displays the oscillatory behavior with the same τ_p as that of diffraction in Fig. 3C.

tation, reaching the lowest value in bulk graphite and the highest one for graphene (32, 34). Extension of these real-time measurements to different length scales, specimens of different density of dislocations, orientations, and the like would allow further exploration of their influences, at the nanoscale, on v, Y, and other properties. We note that selected-area imaging was critical because different regions have temporally different amplitudes and phases across the image. The presence of inhomogeneity on the micrometer scale of the thermoelastic properties of grains in polycrystalline materials is a motif of time-integrated imaging in scanning electron acoustic microscopy (35).

Uniting the power of the spatial resolution of EM with the ultrafast electron timing of UEM enables the unraveling of the elementary dynamics of structures and morphologies in the four dimensions of time and space. With total dissipation of specimen heat between pulses, selected-area dynamics make it possible to study the changes in seconds of recording and for selected pixels of the image. The applications given here, for both gold and graphite in the nonequilibrium state (temperature rate reaching 10¹³ K/s), display a wide range of time and length scales of structure and morphology, as well as ultrafast coherent (resonance) behavior. These examples illustrate the potential for other applications, including nanomechanical

systems (41), especially when incorporating the different and valuable variants of EM that we have in our UEM for physical and biological imaging.

References and Notes

- 1. M. Knoll, E. Ruska, Z. Phys. 78, 318 (1932).
- 2. A. V. Crewe, J. Wall, J. Langmore, Science 168, 1338 (1970).
- 3. M. Haider et al., Nature 392, 768 (1998).
- 4. D. A. Muller et al., Science 319, 1073 (2008).
- P. E. Batson, N. Dellby, O. L. Krivanek, *Nature* 418, 617 (2002).
- 6. K. Kimoto et al., Nature 450, 702 (2007).
- M. A. O'Keefe, *Ultramicroscopy* 108, 196 (2008) and references therein.
- 8. D. J. De Rosier, A. Klug, Nature 217, 130 (1968).
- 9. R. Henderson, Q. Rev. Biophys. 37, 3 (2004).
- 10. V. Lucic, F. Förster, W. Baumeister, Annu. Rev. Biochem. 74, 833 (2005).
- 11. A. Komeili, Z. Li, D. K. Newman, G. J. Jensen, *Science* **311**, 242 (2006).
- 12. W. Jiang et al., Nature 439, 612 (2006).
- 13. X. D. Zou, S. Hovmöller, Acta Crystallogr. A 64, 149 (2008).
- 14. P. W. Hawkes, J. C. H. Spence, Eds., Science of Microscopy (Springer, New York, 2006), vol. 1.
- J. M. Thomas, in *Physical Biology: From Atom to Medicine* A. H. Zewail, Ed. (Imperial College Press, London, 2008).
- A. Howie, P. M. Midgley, C. J. Humphreys, O. Terasaki, in *Turning Points in Solid-State, Materials and Surface Science* K. D. M. Harris, P. P. Edwards, Eds. (Royal Society of Chemistry, Cambridge, 2008).
- 17. E. D. Boyes, P. L. Gai, Ultramicroscopy 67, 219 (1997).
- 18. A. H. Zewail, *Annu. Rev. Phys. Chem.* **57**, 65 (2006) and references therein.
- 19. H. Dömer, O. Bostanjoglo, Rev. Sci. Instrum. 74, 4369 (2003).
- 20. T. Lagrange et al., Acta Mater. **55**, 5211 (2007).

- A. Gahlmann, S. T. Park, A. H. Zewail, *Phys. Chem. Chem. Phys.* 10, 2894 (2008).
- H. S. Park, J. S. Baskin, O.-H. Kwon, A. H. Zewail, Nano Lett. 7, 2545 (2007).
- 23. O.-H. Kwon *et al.*, *Proc. Natl. Acad. Sci. U.S.A.* **105**, 8519 (2008)
- A. H. Zewail, V. A. Lobastov, Method and system for ultrafast photo-electron microscope, US Patent 7,154,091 B2, 20050401 (2006).
- A. H. Zewail, in Visions of Discovery: Shedding New Light on Physics and Cosmology, R. Chiao, W. Phillips,
 A. Leggett, M. Cohen, G. Ellis, D. York, R. Bishop, C. Harper, Eds. (Cambridge University Press, Cambridge, 2008), chap. 2.
- B. Fultz, J. M. Howe, Transmission Electron Microscopy and Diffractometry of Materials (Springer, New York, 2002).
- 27. The deviation from 1 in the correlation of independent measurements for the same real image pattern is a measure of the overall scale of image relief relative to the random noise contribution in the frames. Thus, a flatter image, relative to the noise, will have a smaller γ value for independently recorded frames; see, for example, the slight difference in baseline values in Fig. 2C.
- 28. The width rises because of the induced structural inhomogeneity, as expected, and near t = 0 an initial decrease is noted, which indicates that the overall temporal response is much faster than that of the amplitude or separation rise.
- 29. J. Hohlfeld et al., Chem. Phys. 251, 237 (2000).
- 30. G. Ertl, Adv. Catal. 45, 1 (2000).
- 31. We have calculated the maximum strain-induced tilt angle of the surface normal and found it to be $\phi \simeq \sqrt{6\Delta L/L}$. For $\Delta L/L = 0.043\%$, $\phi = 2.9^{\circ}$, and the corresponding bulge reaches 1 to 10 nm when the local (lateral) deformation scale is 0.08 to 0.8 μm . For the nanosecond heating at a fluence of 40 mJ/cm2 (Fig. 2F), the Bragg spot separation change is ~1%, giving $\phi =$ 14°. The calculated angles correspond well to the angles of microscope specimen tilt needed to produce diffraction and contrast changes similar to those caused by heating. The lateral expansion of $\Delta L/L = 0.043\%$ after fs heating gives, at equilibrium, a temperature change of 30 K, using $\alpha = 14.2 \times 10^{-6} \text{ K}^{-1}$. A higher ΔT derived from the intensity changes (Debye-Waller factor) may have some contribution from zone-axis tilt. Because the zone axis was along the [100] direction before the arrival of the heat impulse, the influence of tilting would make the derived ΔT a maximum value.
- O. L. Blakslee, D. G. Proctor, E. J. Seldin, G. B. Spence,
 T. Weng, J. Appl. Phys. 41, 3373 (1970).
- 33. W. N. Reynolds, *Physical Properties of Graphite* (Elsevier, Amsterdam, 1968).
- 34. C. Lee, X. Wei, J. W. Kysar, J. Hone, Science 321, 385 (2008).
- 35. D. G. Davies, Philos. Trans. R. Soc. Lond. A 320, 243 (1986).
- P. B. Hirsch, A. Howie, R. B. Nicholson, D. W. Pashley, M. J. Whelan, *Electron Microscopy of Thin Crystals* (Butterworths, London, 1965).
- 37. F. E. Fujita, K. Izui, J. Phys. Soc. Jpn. 16, 214 (1961).
- S. K. Choudhary, A. K. Gupta, Jpn. J. Appl. Phys. 46, 7450 (2007).
- Z. L. Wang, Elastic and Inelastic Scattering in Electron Diffraction and Imaging (Plenum, New York, 1995).
- D. Shindo, K. Hiraga, High-Resolution Electron Microscopy for Materials Science (Springer-Verlag, Tokyo, 1998)
- 41. O.-H. Kwon et al., Nano Lett. 8, 3557 (2008).
- 42. We thank F. Carbone for his handling of the graphite film and for helpful discussion. This work was supported by the National Science Foundation and Air Force Office of Scientific Research in the Gordon and Betty Moore Center for Physical Biology at Caltech. Research on biological UEM imaging was supported by the National Institutes of Health. Caltech has filed a provisional patent application for the microscope described here.

Supporting Online Material

www.sciencemag.org/cgi/content/full/322/5905/1227/DC1 Fig. S1

Movies S1 and S2

30 July 2008; accepted 22 October 2008 10.1126/science.1164000



4D Imaging of Transient Structures and Morphologies in Ultrafast Electron Microscopy

Brett Barwick, Hyun Soon Park, Oh-Hoon Kwon, J. Spencer Baskin and Ahmed H. Zewail

Science **322** (5905), 1227-1231. DOI: 10.1126/science.1164000

ARTICLE TOOLS http://science.sciencemag.org/content/322/5905/1227

SUPPLEMENTARY http://science.sciencemag.org/content/suppl/2008/11/20/322.5905.1227.DC1 MATERIALS

REFERENCES This article cites 28 articles, 5 of which you can access for free

http://science.sciencemag.org/content/322/5905/1227#BIBL

PERMISSIONS http://www.sciencemag.org/help/reprints-and-permissions

Use of this article is subject to the Terms of Service